Thickness-Dependent Charge-Carrier Mobility in Home-Grown High-Purity Germanium Crystals

Narayan Budhathoki, Dongming Mei,* Sanjay Bhattarai, Sunil Chhetri, Kunming Dong, Shasika Panamaldeniya, Athul Prem, and Austin Warren Department of Physics, University of South Dakota, Vermillion, SD 57069, USA (Dated: November 27, 2025)

Understanding how charge-carrier mobility evolves as high-purity germanium (HPGe) is thinned from bulk to micrometer scale is essential for optimizing advanced radiation detectors, thin-body Ge electronics, and emerging quantum devices. We report, to our knowledge, the first systematic thickness-dependent mobility study on bulk-grown, detector-grade HPGe, performing Hall-effect measurements on n- and p-type samples thinned from 2.7 mm down to 7 μ m at room temperature. The mobility follows an extended-exponential dependence $\mu(t) = \mu_0 \left[1 - \exp \left(- (t/\tau)^{\beta} \right) \right]$ with characteristic electrostatic lengths $\tau = 6-50 \ \mu m$. Comparison with boundary-scattering and depletion-based models shows that mobility degradation is dominated not by Fuchs-Sondheimer surface scattering but by electrostatic depletion that reduces the effective conducting channel thickness. Across all samples, the hierarchy $\lambda_D < \tau \lesssim W_0$ identifies long-range screening and near-surface electric fields as the primary mechanisms governing the mobility crossover. This connection provides a simple device-level design rule: maintaining $t \gtrsim 3\tau$ preserves most of the bulk mobility, while thinner devices enter a depletion-controlled regime with sharply reduced transport. The extracted parameters thus supply quantitative benchmarks for mobility engineering in ultrathin HPGe and a predictive framework for Ge-on-insulator structures, fully depleted channels, and future Ge-based quantum and electronic technologies.

I. INTRODUCTION

High-purity germanium (HPGe) remains a benchmark semiconductor for radiation detection, infrared photonics, and emerging quantum technologies due to its exceptional crystalline purity, high carrier mobility, and narrow band gap[1–4]. These intrinsic properties enable efficient charge collection, low electronic noise, and excellent energy resolution over a wide range of operating conditions, making HPGe indispensable for low-threshold ionization detectors and precision semiconductor devices[5–7].

Beyond detector applications, Ge has re-emerged as a promising channel material for next-generation microelectronics as silicon complementary metal-oxide-semiconductor (CMOS) approaches its electrostatic and mobility scaling limits[8–14]. Ge exhibits the highest hole mobility among group-IV semiconductors ($\mu_h \approx 1900~\text{cm}^2/\text{V}.\text{s}$)[15, 16] and an electron mobility well above that of silicon[17–22], motivating continued development of Ge-on-insulator (GeOI) and ultra-thin-body Ge transistors. In such devices—and in thinned HPGe detectors—the active channel thickness is often reduced to tens of micrometers or below, making it essential to understand how mobility evolves as a function of thickness.

Carrier mobility in thin semiconductors can degrade through several mechanisms, including surface-field-induced depletion, long-range Coulomb scattering, interface disorder, and strain-induced band-structure

modification [23, 24]. While these mechanisms have been extensively characterized in Si, strained-Ge, and GeOI technologies [22, 23, 25], a systematic experimental framework describing thickness-dependent mobility in high-purity, bulk-grown Ge remains largely unexplored. In particular, the interplay between electrostatic screening, depletion width, and intrinsic band anisotropy has not been fully established for mechanically thinned HPGe crystals, where interface-induced scattering is minimal and electrostatic effects are expected to dominate.

Prior studies of mobility in Ge and related systems have largely focused on Ge-on-insulator (GeOI) and ultrathin epitaxial films, where transport is strongly influenced by interface disorder, strain relaxation, and gatestack engineering [13, 22, 24]. These works provide valuable insight into technologically relevant metal-oxidesemiconductor (MOS) and channel structures, but they do not address bulk-grown, detector-grade Ge that is mechanically thinned to the few-micrometer scale while preserving ultra-low impurity levels and minimal interface damage. In contrast, the present work reports the first systematic, thickness-dependent mobility study on bulk high-purity Ge, covering a continuous range from 2.7 mm down to $7 \mu \text{m}$ on the same material platform. This geometry is directly relevant to HPGe detectors, Ge-based quantum sensors, and Ge electronics where devices are thinned for charge-collection speed, phonon engineering, or hybrid integration, yet must retain nearbulk mobility [5, 6, 8].

Classical boundary-scattering models such as the Fuchs-Sondheimer (FS) formalism predict only mild thickness dependence when the mean free path is much smaller than the physical thickness, as is the case for HPGe at room temperature [26, 27]. In contrast, surface

^{*} Dongming.Mei@usd.edu

depletion can substantially reduce the effective conducting thickness when the physical thickness approaches the Debye length, leading to a strong, monotonic suppression of mobility[23]. A unified empirical description that captures this electrostatically governed transition from bulk-like to thin-body transport would therefore be valuable for both detector optimization and the design of advanced Ge-based electronic and quantum devices.

In this work, we experimentally investigate charge-carrier mobility in home-grown HPGe crystals fabricated at the University of South Dakota. Van der Pauw Halleffect measurements were performed on p- and n-type samples thinned from 2.7 mm to 7 μ m. A central outcome is that the measured electron and hole mobilities are accurately described by an extended-exponential law

$$\mu(t) = \mu_0 \left[1 - \exp(-(t/\tau)^{\beta}) \right],$$
 (1)

where μ_0 is the bulk mobility, τ is a characteristic electrostatic screening length, and β quantifies dimensional sensitivity. Comparison with FS-only and depletiononly models shows that boundary scattering is negligible, whereas surface-field-induced depletion dominates the observed thickness dependence. The extracted characteristic lengths satisfy the hierarchy $\lambda_D < \tau \lesssim W_0$, indicating that mobility suppression in HPGe is primarily governed by electrostatic effects rather than diffuse surface scattering. This connection provides a simple device-level design rule: maintaining the active thickness in the regime $t \gtrsim 3\tau$ preserves most of the bulk mobility, whereas devices with $t \lesssim \tau$ enter a depletion-controlled regime with strongly suppressed transport. In this way, the thickness dependence of mobility in ultra-pure Ge is reduced to a small set of physically transparent parameters that can be used directly in detector and device design.

Overall, this study establishes a consistent electrostatic framework for thickness-dependent transport in HPGe, unifying the behavior of micrometer-scale samples with their bulk counterparts. These results provide quantitative guidance for optimizing high-resolution HPGe detectors and designing thin-body Ge-based electronic and quantum devices in which mobility engineering and electrostatic control must be carefully balanced.

II. METHODS

A. Crystal Growth and Material Preparation

High-purity germanium crystals were grown in-house using successive zone refining and Czochralski pulling. Commercial Ge ingots with initial impurity concentrations of $(10^{13}-10^{14})$ cm⁻³ were refined to $(2-3)\times 10^{11}$ cm⁻³[28]. Prior to melting, all components contacting the charge were cleaned in DI water and acetone, followed by an HNO₃:HF (3:1) etch for Ge surfaces and $\rm H_2O_2$ treatment for quartz hardware. The charge was

melted in a quartz crucible on a graphite susceptor using RF induction heating. Chamber pressure was reduced to 20 Pa and subsequently to $\sim 2 \times 10^{-3}$ Pa before stabilization.

Crystal growth proceeded from a $\langle 100 \rangle$ seed. Boules (8–8.5 cm diameter) were pulled at 40 mm/h during necking and 22 mm/h during body growth in 5N H₂. An initial Dash neck suppressed dislocations, followed by constant-diameter growth and a tapered tail-off[28, 29]. The crystals were cooled over a 10 h controlled cycle and removed for characterization.

B. Sample Thinning and Surface Preparation

Samples were thinned using sequential mechanical and chemical processing. Wafers were first sliced using a diamond wire saw and mechanically lapped to approximately 300 μm . Coarse and fine planarization were performed with 10 μm and 5 μm Al_2O_3 abrasives to achieve a uniform surface.

Final thickness control was obtained by iterative wet chemical etching in HF:HNO₃ (1:6), which provides uniform material removal with minimal subsurface damage for HPGe[28]. During etching, each sample was mounted on a PTFE base using Crystalbond wax, which provided mechanical support and resistance to HF. A representative mounting configuration is shown in Fig. 1.

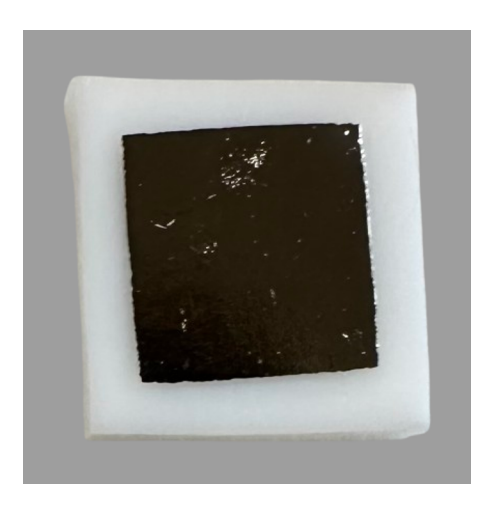


FIG. 1. Representative HPGe sample mounted on a PTFE base using Crystalbond wax for mechanical stability and HF resistance during thinning.

After each etching cycle, samples were rinsed in DI water, dried under nitrogen, and demounted for inspection. Optical microscopy verified the absence of pits or etch-induced defects at the resolution limit, and stylus profilometry confirmed the thickness with a typical uncertainty of $\pm 1~\mu m$. This protocol reproducibly produced samples ranging from the bulk scale 2.7 mm down to $7~\mu m$ without detectable surface deterioration relative to as-grown detector-grade material[28].

C. Thickness Determination

The thickness of each sample was determined using the mass–density–area method. Prior to each thinning step, the sample was cut to a known area ($A \approx 1 \text{ cm}^2$). After each controlled acid etch, the sample was rinsed, dried, and the remaining mass (m) was measured using a 0.1 mg precision balance. Using the density of Ge ($\rho = 5.323 \text{ g/cm}^3$), the instantaneous thickness after each etch was computed as:

$$t = \frac{m}{\rho A}. (2)$$

This approach provided sub-micrometer accuracy throughout the sequential thinning process and was cross-validated against profilometry measurements.

D. Electrical Transport Measurements

Room-temperature (295 K) charge-transport measurements were performed using the Van der Pauw Halleffect method on an Ecopia HMS-3000 system. Four indium-based ohmic contacts were placed at the corners of each HPGe specimen to ensure uniform current distribution and low contact resistance. A representative sample mounted on the carrier board is shown in Fig. 2.

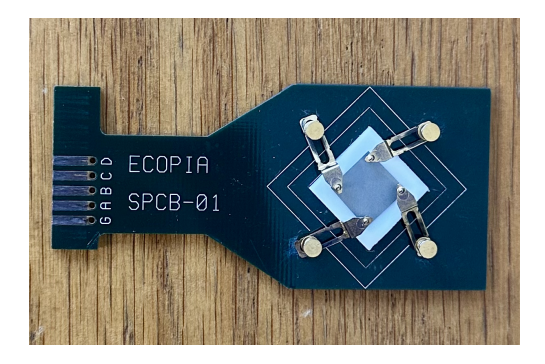


FIG. 2. HPGe sample mounted in a Van der Pauw geometry with four indium corner contacts.

During each measurement, a constant excitation current (1–200 μ A) was applied while a perpendicular magnetic field up to 0.58 T was swept. The transverse Hall voltage V_H and the longitudinal voltage V_x were recorded simultaneously, allowing for the determination of resistivity, carrier density, and Hall mobility. The measurement configuration is illustrated in Fig. 3.

Ohmic behavior and the absence of self-heating were verified by checking that V_x was linear in I_x and that the extracted mobility and carrier concentration were independent of current within experimental uncertainty over the range (1–200 μ A). The resistivity is given by

$$\rho = R_s t, \tag{3}$$

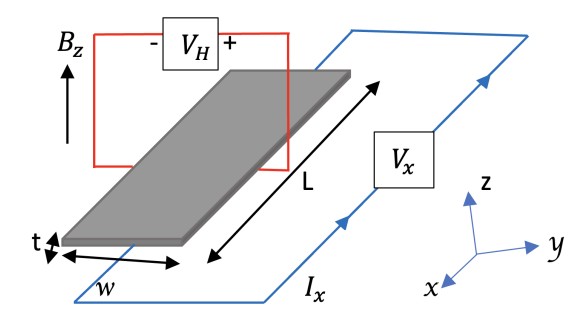


FIG. 3. Hall-effect measurement geometry. A current I_x flows along the x-direction under a perpendicular magnetic field B_z , producing a transverse Hall voltage V_H .

where R_s is the sheet resistance obtained from the Van der Pauw relation and t is the measured sample thickness. The Hall voltage satisfies

$$V_H = -\frac{I_x B_z}{nq t},\tag{4}$$

where q is the elementary charge and n is the carrier concentration. The Hall mobility is obtained from

$$\mu = \frac{1}{qn\rho} = \frac{|V_H|t}{I_x B_z \rho},\tag{5}$$

and the corresponding carrier concentration follows as

$$n = -\frac{I_x B_z}{q \, t \, V_H}.\tag{6}$$

The overall uncertainty in the extracted transport parameters is within $\pm 1\%$, and it is dominated by geometric variations in contact placement and instrument precision. Each mobility value represents the average of at least three independent measurement runs at both magnetic-field polarities to ensure reproducibility.

E. Modeling and Data Analysis

The experimentally measured mobility was fitted using the extended-exponential function in Eq. (1). The extracted characteristic length τ was then compared with the Debye screening length(λ_D),

$$\lambda_D = \sqrt{\frac{\varepsilon k_B T}{q^2 N_{\text{eff}}}},\tag{7}$$

where $N_{\rm eff}$ is the Hall-extracted effective impurity concentration, and with the zero-temperature depletion width W_0 obtained from the electrostatic model discussed in Sec. III.

To benchmark the empirical model, the fitted results were compared with two classical limits: (i) the Fuchs-Sondheimer surface-scattering model, and (ii) a

depletion-only electrostatic model with a field-dependent conducting thickness. Consistent with the data, FS scattering produced negligible thickness dependence, while the depletion model reproduced the dominant observed trend and bounded the fitted values of τ . All visualizations were created using Matplotlib[30]. Uncertainties were propagated using standard Gaussian error propagation, and best-fit parameter errors were obtained from the covariance matrix returned by the fitting routine.

III. RESULTS

A. Characteristic Electrostatic and Transport Scales

The characteristic electrostatic and transport length scales that control thickness-dependent mobility in HPGe are summarized in Table I and plotted in Fig. 4 for all USD-grown samples (P,Q,R,S,X, and Y). Together, they establish a consistent physical hierarchy that constrains how the effective conducting channel evolves as the crystal is thinned.

The Debye screening length ranges from 4–21 μ m across the measured impurity concentrations (5–133) × 10^{10} cm⁻³, decreasing systematically with increasing doping. The surface depletion width (W_0) spans 14–73 μ m over the same range, consistent with typical Ge surface band bending of 0.1–0.3 V. For all samples $W_0 > \lambda_D$, indicating that surface electric fields penetrate deeply into the crystal and can significantly reduce the electrically active thickness. By contrast, the phonon-limited mean free path is only $\lambda_{\rm mfp} \approx 44$ nm, more than three orders of magnitude smaller than the thinnest specimen. Thus, diffuse boundary scattering cannot account for the observed mobility suppression; the condition $t/\lambda_{\rm mfp} \gg 100$ holds for every sample, placing the system firmly in the bulk-scattering regime.

Across the full set of samples, the fitted characteristic length τ obeys the hierarchy

$$\lambda_{\rm mfp} \ll \lambda_D < \tau \lesssim W_0,$$
 (8)

showing that the mobility crossover is governed by electrostatic constraints rather than by boundary scattering. A key result of Fig. 4 is that τ exhibits approximately linear correlations with both λ_D and W_0 .

a. Linear trend between τ and λ_D : A global linear fit for samples (P, Q, R, S, X, and Y) yields

$$\frac{d\tau}{d\lambda_D} \approx 2.55,$$

so that τ increases more than twice as fast as the Debye length. This indicates that the mobility recovery with thickness is strongly screening-driven: as λ_D increases (weaker doping), the surface potential extends further into the bulk and the effective conducting thickness expands accordingly. The slope greater than one implies

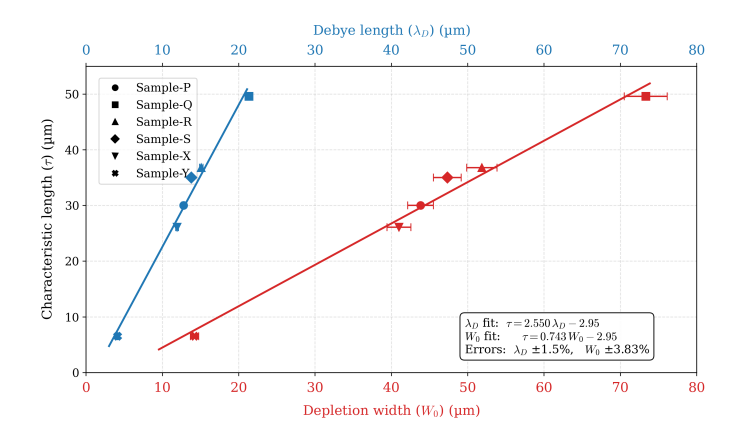


FIG. 4. Electrostatic and transport length scales for USD-grown HPGe samples (P,Q,R,S,X, and Y). Symbols denote the Debye length (λ_D), depletion width (W_0), and fitted mobility characteristic length (τ). Blue (top axis) and red (bottom axis) scales correspond to λ_D and W_0 . Linear fits quantify how the characteristic length τ tracks the electrostatic scales across all samples.

that τ is influenced not only by screening but also by the gradual relaxation of the depletion field.

b. Linear trend between τ and W_0 : A second linear trend appears between τ and the depletion width, with a smaller slope,

$$\frac{d\tau}{dW_0} \approx 0.74.$$

Here τ grows more slowly than the total depleted region, which shows that only a portion of the depletion layer participates in conduction. The characteristic length τ therefore probes a partially depleted, partially screened channel rather than the full depletion width.

c. Interpretation of slope ratio: The ratio

$$\frac{(d\tau/d\lambda_D)}{(d\tau/dW_0)} \approx 3.44$$

demonstrates that τ responds 3.4 times more strongly to changes in the Debye length than to changes in the depletion width. In other words, the mobility crossover is controlled primarily by long-range screening rather than by the absolute size of the depleted region. The persistent ordering $\lambda_D < \tau < W_0$ indicates that τ marks the depth at which surface fields substantially distort the potential, but not necessarily the depth of full depletion.

Taken together, these trends identify τ as an electrostatic thickness scale that interpolates smoothly between screening-controlled and depletion-controlled limits. Its magnitude and scaling behavior provide the physical basis for the extended-exponential mobility law used in the following subsections and for the design rule $t\gtrsim 3\tau$ that preserves near-bulk mobility.

experimental samples shown in Fig. 4.			
Model / Scale	Governing expression	Representative inputs	Value / Interpretation
Debye length, λ_D	$\lambda_D = \sqrt{\frac{\varepsilon k_B T}{q^2 n}}$	$\varepsilon_r = 16.2, T = 295 \text{ K}, n = (5-133) \times 10^{10} \text{ cm}^{-3}$	$\lambda_D = 421~\mu\mathrm{m}$ (decreases with $N_{\mathrm{eff}})$
Surface depletion width, W_0	$W_0 = \sqrt{\frac{2\varepsilon(V_{bi} - V)}{2\varepsilon(V_{bi} - V)}}$	$(V_{bi} - V) = 0.1 - 0.3 \text{ V}, N = (5 - 133) \times 10^{10} \text{ cm}^{-3}$	$W_0=1473~\mu\mathrm{m};$ always $>\lambda_D$
Mean free path, λ_{mfp}	$\lambda_{\rm mfp} = \frac{\mu_0 m^* v_{th}}{q}$ $\mu(t) = \mu_0 [1 - e^{-(t/\tau)^{\beta}}]$	$\mu_0 = 1900 \text{ cm}^2/\text{V} \cdot \text{s}, \ m_e^* = 0.12 m_0$	$\lambda_{\rm mfp} \approx 44$ nm (phonon-limited)
Empirical mobility fit (holes)	$\mu(t) = \mu_0 [1 - e^{-(t/\tau)^{\beta}}]$	$\mu_0 = 1899.1 \text{ cm}^2/\text{N} \cdot \text{s}, \tau = 40.4 \mu\text{m}, \beta = 1.12$	$ au > \lambda_D$
Empirical mobility fit (electrons)	$\mu(t) = \mu_0 [1 - e^{-(t/\tau)^{\beta}}]$	$\mu_0 = 2349.2 \text{ cm}^2/\text{N} \cdot \text{s}, \ \tau = 24.6 \ \mu\text{m}, \ \beta = 0.59$	$ au > \lambda_D$
Fuchs-Sondheimer scattering	$\mu(t) \approx \mu_0 \left[1 - \frac{3\lambda_{\text{mfp}}}{8t} (1-p)\right]$	$p \in [0, 1]$ (specularity factor)	Negligible for $t > 10 \ \mu \mathrm{m}$

TABLE I. Characteristic electrostatic and transport scales for HPGe at T=295 K. Parameters are representative of the experimental samples shown in Fig. 4

Thickness-Dependent Mobility Behavior

Figures 5 and 6 show the measured hole and electron mobilities as a function of crystal thickness for all USD-grown samples. In the bulk regime $(t > 100 \ \mu \text{m})$, both carrier types asymptotically approach their intrinsic room-temperature limits,

$$\mu_{0,h} \approx 1.899 \times 10^3 \text{ cm}^2/\text{V.s}, \qquad \mu_{0,e} \approx 2.349 \times 10^3 \text{ cm}^2/\text{V.s},$$

consistent with established benchmarks for ultrapure Ge[4, 16, 31]. In this regime, carrier motion is dominated by phonon scattering and is essentially independent of thickness.

Below $t \approx 100 \ \mu \text{m}$, the mobility decreases sharply as the electrically active thickness becomes comparable to the electrostatic screening length. This suppression originates from the reduction of the undepleted channel thickness by long-range surface fields, band bending, and Coulomb scattering associated with near-surface spacecharge regions.

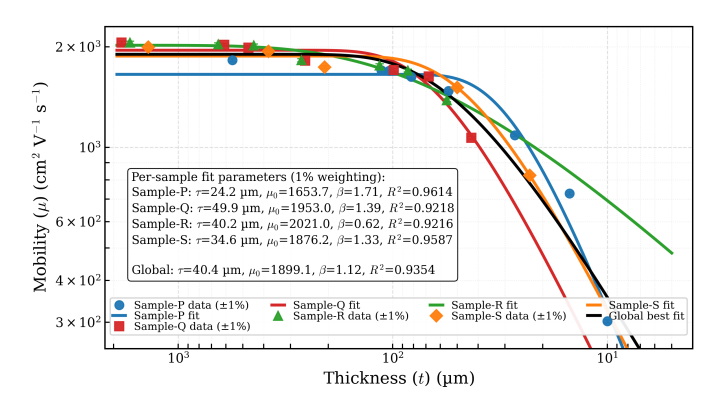


FIG. 5. Hole mobility for USD-grown p-type HPGe Samples (P,Q,R, and S). Symbols: measured data ($\pm 1\%$). Colored curves: individual extended-exponential fits. Black curve: global fit. All samples exhibit a smooth crossover from thin, screening-limited transport to bulk-like behavior.

The extended-exponential model reproduces the mobility data for all samples with $R^2 > 0.92$. For holes

(Samples P, Q, R, and S), the global best-fit parameters are $\mu_0 = 1899.1 \text{ cm}^2/\text{V.s}, \tau_h = 40.4 \mu\text{m}, \text{ and}$ $\beta_h = 1.12$. For electrons (X, Y), the corresponding values are $\mu_0 = 2349.2 \text{ cm}^2/\text{V.s}$, $\tau_e = 24.6 \mu\text{m}$, and $\beta_e = 0.59$. The smaller τ_e and β_e reflect shorter screening lengths and weaker band-structure sensitivity of the conduction band, consistent with the reduced thickness sensitivity of electron transport.

Across all samples, the similarity between τ and the calculated Debye length λ_D confirms that the mobility crossover is governed primarily by electrostatic depletion rather than interface roughness or boundary scattering. In practical terms, keeping t several times larger than τ ensures that the mobility remains within a few percent of its bulk value.

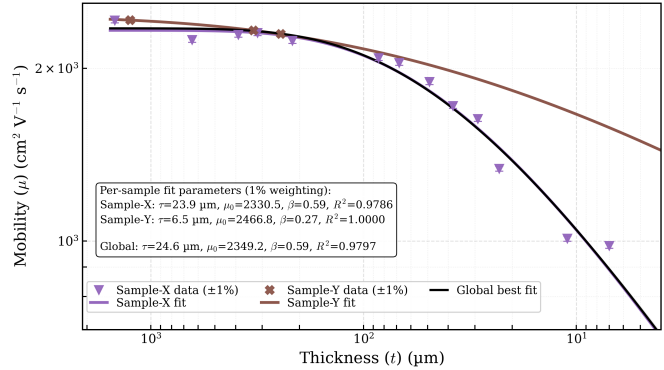


FIG. 6. Electron mobility for USD-grown n-type HPGe Samples (X, and Y). Symbols: measured data. Black curve: global extended-exponential fit.

Model Validation

The extended-exponential description was benchmarked against two classical limiting cases: a Fuchs-Sondheimer (FS-only) boundary-scattering model, and (ii) a depletion-only electrostatic model. Figures 7 and 8 show these comparisons.

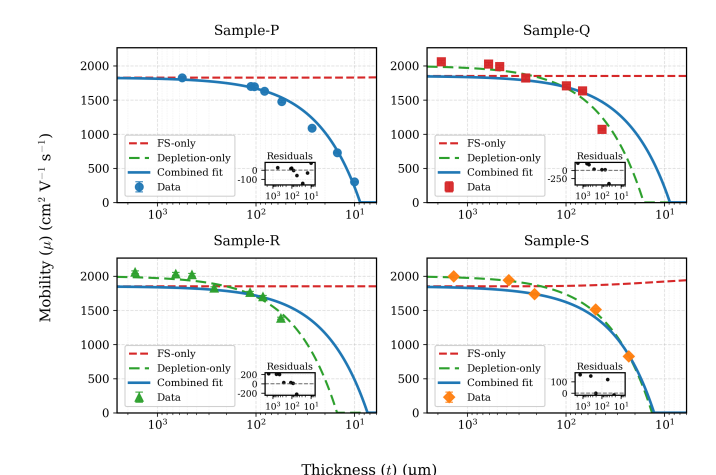


FIG. 7. Model comparison for p-type mobility of samples (P, Q, R, and S). The FS-only model (red dashed) predicts almost thickness-independent mobility. The depletion-only model (green) captures the qualitative trend but misses the curvature at small thickness. The extended-exponential model (blue solid) yields minimal, structureless residuals (inset).

For thick samples ($t \gtrsim 100~\mu\mathrm{m}$), all models converge to the same bulk limit. As thickness decreases, the FS-only model fails completely: because λ_{mfp} is so short, it predicts only a weak, nearly linear correction that cannot reproduce the strong mobility suppression. The depletion-only model produces the correct qualitative trend but systematically underestimates the steep curvature of the experimental roll-off, especially in the $t \lesssim 50~\mu\mathrm{m}$ regime. The extended-exponential model, by contrast, matches the data across the full thickness range with small, non systematic residuals. The fitted values of τ_h and τ_e lie between λ_D and W_0 , in agreement with the hierarchy in Eq. (8) and Fig. 4. This confirms that the mobility suppression in HPGe is governed by electrostatic depletion of the active layer rather than by boundary scattering.

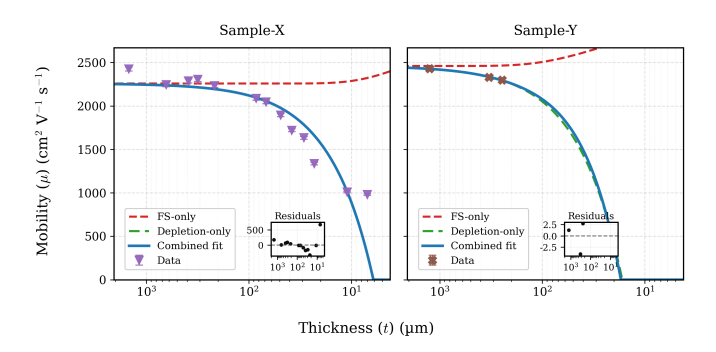


FIG. 8. Model comparison for electron mobility of samples (X, and Y). Only the extended-exponential model captures both the high-t saturation and steep low-t suppression, with small residuals (inset).

Overall, these results show that a single compact functional form captures the electrostatically controlled crossover from depletion-limited to bulk-like transport in HPGe. The parameters μ_0 , τ , and β provide a physically meaningful and device-ready parametrization for mobility engineering in ultrathin Ge detectors and electronic or quantum devices.

IV. DISCUSSION

The measured thickness-dependent mobilities establish a clear transition in high-purity Ge from bulk, phonon-limited transport to an electrostatically confined conduction regime at T=295 K. In the thick-sample limit ($t\gtrsim 100~\mu{\rm m}$), the extracted mobilities, $\mu_{0,h}\approx 1.899\times 10^3~{\rm cm^2/V}$.s and $\mu_{0,e}\approx 2.349\times 10^3~{\rm cm^2/V}$.s, agree with well-established intrinsic values[16, 23, 31], confirming that carrier momentum relaxation is dominated by acoustic and optical phonons when the thickness greatly exceeds all microscopic length scales.

A central result of this study is that the sharp mobility suppression observed for $t < 100~\mu \rm m$ cannot be attributed to classical diffuse boundary scattering. The phonon-limited mean free path, $\lambda_{\rm mfp} \approx 44~\rm nm$, remains more than three orders of magnitude smaller than the thinnest samples. Consequently, all specimens lie well outside the geometric-confinement regime in which the Fuchs–Sondheimer (FS) model is applicable. This explains the failure of the FS-only prediction in Figs. 5–8, which incorrectly yields an almost thickness-independent mobility.

Instead, the mobility crossover is governed by electrostatic effects. The characteristic lengths extracted from the extended-exponential fits, $\tau_h \approx 40.4~\mu \mathrm{m}$ and $\tau_e \approx 24.6~\mu \mathrm{m}$, fall between the Debye screening length λ_D and the depletion width W_0 , obeying

$$\lambda_{\rm mfp} \ll \lambda_D < \tau \lesssim W_0.$$

This hierarchy directly links the mobility roll-off to long-range surface electric fields, which reduce the undepleted channel thickness and constrain the volume available for current flow. The linear trends in Fig. 4 further quantify this behavior: τ increases with λ_D with a slope larger than 2, indicating that mobility recovery is strongly controlled by electrostatic screening, while its weaker dependence on W_0 reflects the partial, but not complete, occupation of the depletion region by mobile carriers.

The fitted exponents ($\beta_h = 1.12$, $\beta_e = 0.59$) capture the distinct band-structure responses of holes and electrons. The sublinear β_e reflects the weaker nonparabolicity and anisotropy of the Ge conduction band, while $\beta_h > 1$ is consistent with the strongly warped valence band and its enhanced sensitivity to electrostatic confinement[32, 33]. Although these parameters are extracted from micrometer-scale samples, where quantum-well subband formation is absent, the pair (τ, β) provides an effective, coarse-grained description of how band structure and electrostatics jointly shape the thickness dependence of mobility at room temperature.

A. Extrapolation toward the nanoscale limit

While chemical–mechanical thinning cannot reliably produce nanometer-thick HPGe layers with atomically smooth surfaces, the experimentally observed trends allow a physically grounded extrapolation toward the nanoscale. The strong correlation between τ and λ_D for lightly doped samples (P, Q, R, and S) implies that reducing the thickness into the few-tens-of-nanometers range would place the entire film within the electrostatic screening region; in this limit, mobility is dictated directly by the surface potential profile and should fall rapidly as t approaches λ_D .

For the more heavily doped samples (X, and Y), the weaker τ - W_0 slope shows that the conduction channel is already highly compressed by the surface-space-charge field. As t approaches the mean free path $(t \sim \lambda_{\rm mfp})$, surface-scattering mechanisms, negligible at micrometer thickness, are expected to become dominant, leading to a transition toward boundary-limited transport consistent with ultrathin Ge films and Ge-on-insulator structures [34, 35]. In this sense, the present results bridge the regime where electrostatic confinement dominates (micrometer-scale HPGe) and the regime where both electrostatics and surface scattering control mobility in truly nanoscale Ge. A full treatment of the lowtemperature case, where mean free paths become longer and additional decoherence channels appear, is left for future work.

B. Device implications

These findings have direct consequences for HPGe detectors, thin-film electronics, and quantum devices. For low-threshold radiation detectors, thinning below a few times the characteristic length τ significantly reduces mobility, increasing carrier transit time and electronic noise. Maintaining the active thickness in the regime $t \gtrsim 3\tau$ preserves most of the bulk mobility, whereas devices with $t \lesssim \tau$ operate in a depletion-controlled regime with sharply degraded transport. In practice, this can be addressed by keeping critical drift regions thicker than the electrostatic scale or by mitigating surface fields through passivation, dielectric engineering, and optimized contact geometries.

For emerging nanoscale Ge-based platforms, including phonon-coupled quantum sensors and Ge qubits, the results show that impurity control alone is insufficient: precise engineering of the surface potential and depletion geometry is essential to prevent severe mobility loss at reduced dimensions. The parameters (μ_0, τ, β) extracted here thus serve as a compact, device-level design rule for estimating mobility penalties in the thinned Ge under realistic electrostatic conditions.

In summary, this work establishes a quantitative and physically grounded framework linking Debye screening, depletion geometry, and thickness-dependent mobility in HPGe at room temperature. By connecting the parameters of the extended-exponential model to fundamental electrostatic scales, we provide a compact description of the transition from bulk phonon-limited transport to electrostatically confined conduction. These insights inform the optimization of Ge-based detectors and ultrathin semiconductor devices that operate at the boundary between bulk and mesoscale physics and provide a starting point for future extensions to cryogenic operation and quantum architectures.

V. CONCLUSION

We have experimentally established the thickness dependence of charge-carrier mobility in HPGe over a wide range of micrometer-scale thicknesses at room temperature. The data reveal a clear transition from bulk, phonon-limited transport to an electrostatically confined conduction regime as the crystal is thinned. The measured mobilities cannot be described by classical diffuse boundary scattering: the phonon-limited mean free path remains orders of magnitude smaller than the physical thickness for all samples. Instead, the characteristic lengths extracted from an extended-exponential model satisfy

$$\lambda_{\rm mfp} \ll \lambda_D < \tau \lesssim W_0$$

demonstrating that mobility suppression is governed primarily by Debye screening and surface depletion rather than geometric confinement.

The strong linear correlation between τ and λ_D in lightly doped samples, together with the weaker τ – W_0 relation in more heavily doped material, quantifies how the effective conducting channel evolves with doping and surface band bending. These trends show that the mobility crossover reflects the depth of the electrostatic perturbation into the crystal rather than interface roughness. The fitted exponents (β_h, β_e) further encode the distinct valence- and conduction-band responses to electrostatic confinement and provide an effective, band-structure-aware description of thickness-dependent transport.

Although our measurements are confined to the micrometer regime, the observed hierarchy of length scales provides a physically grounded path to extrapolate toward nanoscale Ge. As thickness approaches tens of nanometers, the conducting volume becomes fully confined within the screening region and transport is expected to evolve from purely electrostatic limitation toward a regime where surface scattering also contributes significantly, consistent with behavior reported in epitaxial and Ge-on-insulator ultrathin films. Extending this framework to cryogenic temperatures, where mean free paths and additional decoherence channels change, is a natural direction for future work.

Overall, this study provides a compact, quantitative framework connecting Debye screening, depletion geometry, and thickness-dependent mobility in HPGe. The extended-exponential model, with parameters (μ_0, τ, β) tied to fundamental electrostatic scales, offers a physically meaningful parametrization of transport from bulk to mesoscale dimensions and a practical design rule: maintaining $t \gtrsim 3\tau$ preserves near-bulk mobility, while $t \lesssim \tau$ pushes devices into a depletion-controlled regime. These insights directly inform the optimization of Gebased radiation detectors, thin-film electronics, and emerging quantum-sensitive devices that must maintain high mobility in confined geometries.

AUTHOR CONTRIBUTIONS

N. Budhathoki performed sample fabrication, surface processing, Hall-effect measurements, data analysis, and manuscript preparation. D.-M. Mei provided conceptual guidance, supervision, and theoretical interpretation. S. Bhattarai, S. Chhetri, K. Dong, S. Panamaldeniya, A. Prem, and A. Warren contributed to crystal growth and material preparation.

- L. S. Darken and C. E. Cox, in *Semiconductors and Semimetals*, Semiconductors and Semimetals, Vol. 43, edited by T. E. Schlesinger and R. B. James (Elsevier, 1995) pp. 23–83.
- [2] G. F. Knoll, Radiation Detection and Measurement, 4th ed. (Wiley, 2010).
- [3] G. Gilmore, Practical Gamma-ray Spectroscopy, 2nd ed. (Wiley, 2008).
- [4] Y. Nakano, H. Morii, and T. Sato, Journal of Crystal Growth 530, 125252 (2020).
- [5] D. M. Mei, S. A. Panamaldeniya, K. Dong, S. Bhattarai, N. Budhathoki, and A. Warren, Quantum Science and Technology 10, 045067 (2025).
- [6] D.-M. Mei, N. Budhathoki, S. A. Panamaldeniya, K.-M. Dong, S. Bhattarai, A. Warren, A. Prem, and S. Chhetri, Physics of the Dark Universe 50, 102165 (2025).
- [7] N. Budhathoki, D. Mei, P. Francisco, and S. Panamaldeniya, in American Physical Society – Global Physics Summit 2025 (APR-V11/7) (2025).
- [8] T. Wei, Z. Han, X. Zhong, Q. Xiao, T. Liu, and D. Xiang, iScience 25, 105160 (2022).
- [9] C. H. Lee, T. Nishimura, T. Tabata, S. K. Wang, K. Nagashio, K. Kita, and A. Toriumi, in 2010 International Electron Devices Meeting (IEDM) (2010) pp. 18.1.1– 18.1.4.
- [10] C. H. Lee, T. Nishimura, K. Nagashio, K. Kita, and A. Toriumi, IEEE Transactions on Electron Devices 58, 1295 (2011).
- [11] R. Zhang, N. Taoka, P.-C. Huang, M. Takenaka, and S. Takagi, in 2011 International Electron Devices Meeting (IEDM) (2011) pp. 28.3.1–28.3.4.
- [12] J. J. Gu, Y. Q. Liu, M. Xu, G. K. Celler, R. G. Gordon, and P. D. Ye, Applied Physics Letters 97, 012106 (2010).
- [13] C. H. Lee, T. Nishimura, T. Tabata, D. Zhao, K. Nagashio, and A. Toriumi, Applied Physics Letters 102, 232107 (2013).

ACKNOWLEDGMENTS

This work was supported in part by the National Science Foundation (NSF) under Grants No. NSF OISE-1743790, NSF PHYS 2117774, NSF OIA 2427805, NSF PHYS-2310027, and NSF OIA-2437416, and by the U.S. Department of Energy (DOE) under Grants No. DE-SC0024519 and DE-SC0004768. Additional support was provided by a research center funded by the State of South Dakota.

DATA AVAILABILITY

The data that support the findings of this study are available from the corresponding author upon reasonable request.

- [14] S. Takagi, T. Iizawa, T. Tezuka, T. Numata, S. Nakaharai, N. Hirashita, Y. Moriyama, K. Usuda, E. Toyoda, S. Dissanayake, M. Shichijo, R. Nakane, S. Sugahara, M. Takenaka, and N. Sugiyama, IEEE Transactions on Electron Devices 55, 21 (2008).
- [15] M. Myronov, C. Morrison, J. Halpin, S. Rhead, C. Casteleiro, J. Foronda, V. A. Shah, and D. Leadley, Japanese Journal of Applied Physics 53, 04EH02 (2014).
- [16] C. Jacoboni and L. Reggiani, Reviews of Modern Physics 55, 645 (1983).
- [17] D. S. Yu, A. Chin, C. C. Liao, C. F. Lee, C. F. Cheng, M. F. Li, W.-J. Yoo, and S. P. McAlister, IEEE Electron Device Letters 26, 118 (2005).
- [18] J. Feng, G. Thareja, M. Kobayashi, S. Chen, A. Poon, Y. Bai, P. B. Griffin, S. S. Wong, Y. Nishi, and J. D. Plummer, IEEE Electron Device Letters 29, 805 (2008).
- [19] L. Hutin, C. Le Royer, J.-F. Damlencourt, J.-M. Hartmann, H. Grampeix, V. Mazzocchi, C. Tabone, B. Previtali, A. Pouydebasque, M. Vinet, and O. Faynot, IEEE Electron Device Letters 31, 234 (2010).
- [20] T. Maeda, K. Ikeda, S. Nakaharai, T. Tezuka, N. Sugiyama, Y. Moriyama, and S. Takagi, IEEE Electron Device Letters 26, 102 (2005).
- [21] K. Morii, T. Iwasaki, R. Nakane, M. Takenaka, and S. Takagi, IEEE Electron Device Letters **31**, 1092 (2010).
- [22] D. Kuzum, T. Krishnamohan, A. Nainani, Y. Sun, P. A. Pianetta, H.-S. P. Wong, and K. C. Saraswat, IEEE Transactions on Electron Devices 58, 59 (2011).
- [23] M. V. Fischetti and S. E. Laux, Journal of Applied Physics 80, 2234 (1996).
- [24] Y. Nakano, T. Sato, and H. Morii, Journal of Crystal Growth 451, 63 (2016).
- [25] T. Ando, A. B. Fowler, and F. Stern, Reviews of Modern Physics 54, 437 (1982).
- [26] K. Fuchs, Proceedings of the Cambridge Philosophical Society 34, 100 (1938).

- [27] E. H. Sondheimer, Advances in Physics $\mathbf{1}$, 1 (1952).
- [28] S. Bhattarai, D. Mei, N. Budhathoki, K. Dong, and A. Warren, Crystals 14, 177 (2024).
- [29] W. C. Dash, Journal of Applied Physics 29, 736 (1958).
- [30] J. D. Hunter, Computing in Science & Engineering 9, 90 (2007).
- [31] M.-S. Raut, H. Mei, D.-M. Mei, S. Bhattarai, W.-Z. Wei, R. Panth, P. Acharya, and G.-J. Wang, Journal of Instrumentation 15 (10), T10010.
- [32] J. M. Luttinger and W. Kohn, Physical Review 97, 869 (1955).
- [33] G. L. Bir and G. E. Pikus, Symmetry and Strain-Induced Effects in Semiconductors (Wiley, 1974).
- [34] O. Nakatsuka, K. Tsunemasu, Y. Shimura, K. Kutsukake, and S. Zaima, Applied Physics Letters 115, 042101 (2019).
- [35] T. Imajo, T. Suemasu, and K. Toko, Scientific Reports 11, 8333 (2021).